Applied Thermal Engineering 111 (2017) 968–980

Contents lists available at ScienceDirect

Applied Thermal Engineering

journal homepage: www.elsevier.com/locate/apthermeng

Research Paper

Numerical study of film cooling over a flat plate with anisotropic thermal conductivity

Zecan Tu [a], Junkui Mao [a,b,*], Xingsi Han [a]

[a] Jiangsu Province Key Laboratory of Aerospace Power System, College of Energy and Power Engineering, Nanjing University of Aeronautics and Astronautics, Nanjing 210016, PR China
[b] Collaborative Innovation Center for Advanced Aero-Engine, Beijing 100191, PR China

HIGHLIGHTS

- Film cooling over a flat plate with anisotropic thermal conductivity was investigated.
- The variations of the main direction in thermal conductivities were accounted for.
- Both the mean value of cooling effectiveness and its distribution uniformity were examined.
- Cooling performances in different special regions on the target surface were discussed.

ARTICLE INFO

Article history:
Received 24 March 2016
Revised 13 September 2016
Accepted 30 September 2016
Available online 1 October 2016

Keywords:
Film cooling
Anisotropic thermal conductivity
Numerical simulation
Cooling effectiveness

ABSTRACT

Numerical study was performed to investigate the film cooling performance for a flat plate with anisotropic thermal conductivity where the plate had a single row of round holes. The cooling effectiveness and temperature distribution were analyzed and compared between the results of isotropic and anisotropic plates. The effects of two angles on the cooling effectiveness were studied, i.e. the axial angle α (0°, 30°, 35°, 60° and 90°) and the spanwise angle β (0°, 30°, 60° and 90°), with regards to the inclined angle between the main thermal conductivity in the plate and the mainstream flow direction. The results obtained showed that the anisotropy of the thermal conductivity and the inclined angles affected the cooling effectiveness in a complex way. The highest average cooling effectiveness could be achieved with a specific α or β, depending on the downstream region of the film cooling hole being considered. With the blowing ratio Br = 0.5, the highest cooling effectiveness averaged over the 0–5D and 0–20D downstream regions (with D the diameter of the film cooling hole) could be obtained with an angle of around 35° and 90° for α, respectively. It was found that the uniformity of the cooling effect was improved with a larger β. Moreover, the effects of α and β on the average cooling effectiveness were found to be similar with different Br. However, the uniformity was affected by α and β non-monotonically in different cases of Br. This work demonstrates that proper inclined angle can lead to better film cooling performance.

1. Introduction

Better performance for gas turbine engines requires a higher inlet temperature, which could be far beyond 1800 K [1]. However, the performance of a turbine engine could be weakened if too much air is used for cooling. Furthermore, the structures of the hot components would become very complicated when complex cooling configurations are applied (such as impinging cooling, film cooling or internal serpentine cooling channels with ribs and fins). In recent years, the development and implementation of highly heat-resistant materials, such as ceramic matrix composite (CMC), thus have attracted increasing attentions [2–4].

Due to the complications in manufacturing the CMC hot components of a turbine engine [5,6], it is difficult to apply complex (although effective) internal cooling configurations, such as the small ribbed channel or the U type serpentine tube configurations. Alternatively, film cooling may be applied, which is simpler and easier to implement. It bleeds internal coolant onto the exterior hot surface and forms a thin cooling film. This thin film can reduce the temperature of the material and protect the surface from hot mainstream. For example, NASA has applied film cooling with round holes on a CMC vane and it passed the engineering tests successfully [7]. The entire battery of tests included fifty hours of

* Corresponding author at: Jiangsu Province Key Laboratory of Aerospace Power System, College of Energy and Power Engineering, Nanjing University of Aeronautics and Astronautics, Nanjing 210016, PR China
E-mail address: mjkpe@nuaa.edu.cn (J. Mao).

http://dx.doi.org/10.1016/j.applthermaleng.2016.09.170
1359-4311/

Nomenclature

D	diameter of the film hole [mm]	P_{out}	static pressure at the mainstream outlet [Pa]
X, Y, Z	global Cartesian coordinates	k	thermal conductivity [W/(m K)]
ζ, η, ν	local Cartesian coordinates	T	temperature [K]
α	inclined angle between X and ζ axis on X-Z plane	Br	blowing ratio
β	inclined angle between X and ζ axis on X-Y plane	η_{aw}	adiabatic cooling effectiveness
u_∞	velocity of the mainstream inlet [m/s]	η	adiabatic cooling effectiveness
ρ_∞	density of the mainstream [kg/m^3]	$\overline{\eta}$	average cooling effectiveness
u_c	velocity of the coolant flow at the inlet of film hole [m/s]	σ	standard deviation of cooling effectiveness
ρ_c	density of the coolant flow at the inlet of film hole [kg/m^3]		

steady state operation and 102 2-min thermal cycles from 1173 K to 1713 K.

There have been extensive studies on traditional film cooling in the past 40 years. Various aspects of film cooling have been studied, such as the discrete-hole arrangement [8], interactions between the film outflow and the mainstream [9], the vortex structures and evolution [10]. To improve the coverage of a coolant's thin film, Goldstein et al. [11], Ghorab [12] and Yusop et al. [13] studied the axial-shaped film holes with different lateral diffusion degrees. Azzi and Jubran [14] and Yao and Zhang [15,16] focused on novel film cooling configurations with converging slot-holes. All those results showed that the shaped film holes could lead to a better lateral spreading of the coolant, which can improve its coverage and enhance its cooling effectiveness. However, there were still some regions left that the thin film could not cover, which resulted in non-uniform distributions of the temperature on the target hot surface.

The temperature on the target surface may also be affected by the thermal conduction inside the solid material. Film cooling with heat conduction in a solid region is a well-known conjugated heat transfer problem [17]. Silieti et al. [18] conducted a numerical comparison for the adiabatic and conjugated heat transfer of fan-shaped film cooling, where the stainless steel was used as the solid material in the conjugated cases. It was found that the coolant jet was heated and the wall temperature became lower than that of the adiabatic case due to the thermal conduction in the solid. Ai and Fletcher [19] studied the conjugated heat transfer in the regions very close to the film hole (besides the further downstream regions). Their results indicated that the heat was transferred from the solid to the fluid in the region close to the film hole, as the coolant had a lower temperature compared to that of the wall. In contrast, in the further downstream region, heat was transferred from the fluid to the solid, since the coolant mixed with the hot gas and had a higher temperature. Similar studies can also be found in the literatures [20–22].

All of the studies mentioned above used homogeneous materials whose thermal conductivities are isotropic. However, a fiber reinforced composite (FRC), such as the CMC, is of particular interest in the present study since it has anisotropic thermal conductivity - this conductivity results from different thermal properties of the fibers and the matrix, the random distribution of the fibers and the defects introduced in the manufacturing process.

Mutnuri's experiment [23] examined the thermal conductivity of a carbon/vinyl ester composite. It was found that the effective thermal conductivity (ETC) along the longitudinal direction was almost twice as that along the transverse direction, and four times larger than that along the through-the-thickness direction. Additionally, with the fiber volume fraction increasing from 60% to 75%, it almost doubled the conductivity (from 1.035 W/m K to 2.407 W/m K) along the longitudinal direction. Tian and Kevin [24] studied the ETC of a carbon-fiber/epoxy composite by the 3ω method and found that the in-plane and through-thickness thermal conductivities of the sample were 6.316 W/m K and 0.611 W/m K, respectively. Behzad [25] and Xu [26] observed significant anisotropic thermal conductivities and their results showed that the orientation and distribution of the fibers inside the composite affected the ETC significantly.

Borca-Tasciuc et al. [27] presented a detailed analysis and mathematical modeling of the 3ω method which considered the effects of finite substrate thickness, anisotropic nature of the film and substrate thermal conductivity. Zhu and Ertekin [28] studied the phonon transport on two-dimensional graphene/borom nitride superlattices. The underlying mechanism was presented and the thermal transport in anisotropic materials was discussed. It was found that the anisotropic thermal conductivity depends critically on interface topology. Zhu and Ye [29], Liu et al. [30] and Xu [31] also performed theoretical and numerical studies of the non-equilibrium gaseous heat transport in thin films and through small holes. The corresponding numerical method was established.

Therefore, the temperature fields for the hot components made of composites (such as CMC) are significantly different from those made of homogeneous metals due to their anisotropic thermal conductivities. Yusop et al. [32] conducted a numerical study on the film cooling effectiveness of a multi-layer convex surface, where the thermal conductivity was larger than the others in one specific direction. They found that there were significant differences in the temperature distribution (and, hence, the cooling effectiveness) on the convex surface among the multi-layer conjugated cases, one-layer conjugated cases and adiabatic cases.

Despite that extensive studies have examined various aspects of film cooling, there are few work that report on detailed effects of anisotropic thermal conductivity on the film cooling effectiveness, especially under the conditions that large differences exist among the ETCs along different directions. The present work aims to a further understanding of the heat transfer in a composite with film cooling and investigates the effects of anisotropic thermal conductivity on the film cooling performance. The typical long fiber reinforced composite and the traditional single row of round film holes are selected in the present numerical study. The non-uniform temperature distribution was examined, which resulted from the discrete film cooling that further intensified due to the anisotropic thermal conductivity of the composite. The influence of the inclined angle between the principal direction of the thermal conductivity and the mainstream flow direction was also investigated.

2. Numerical methodology

2.1. Physical model and computational domain

A schematic of the flat plate with a single row of round holes, which was made from an ideal long fiber reinforced composite as shown in Fig. 1(a), was taken as an example to show the

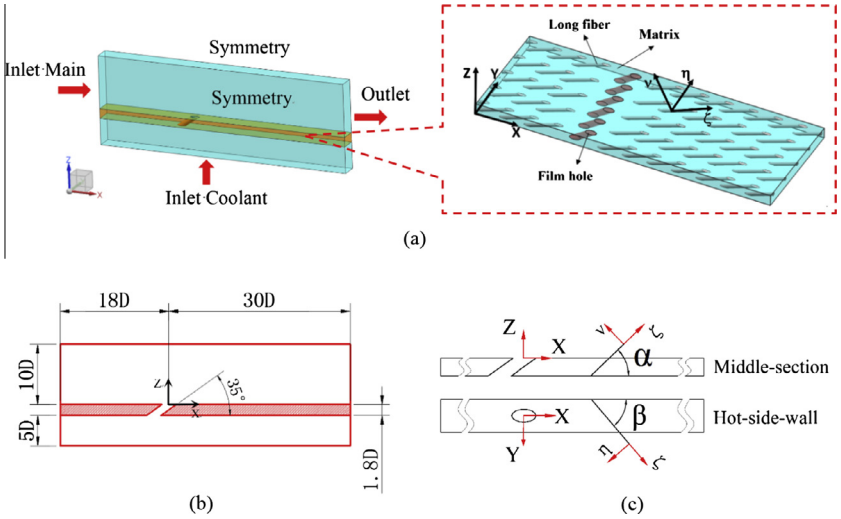

Fig. 1. Schematic of the physical model and the computational domain: (a) the local coordinates of PDTC and the global coordinates; (b) the computational domain; (c) inclined angles.

anisotropic thermal conductivity of FRC. A local Cartesian coordinate (ζ, η, ν) was introduced, with the ζ axis along the central axis of the cylindrical fibers. The ζ axis was considered to be the principal direction of the thermal conductivity (PDTC) in this paper, as the thermal conductivity was largest in this direction. If the PDTC was not along the X axis, there existed an inclined angle between the local Cartesian coordinate (ζ, η, ν) and the global Cartesian coordinate (X, Y, Z). Here, it was referred to as the "inclined angle of PDTC".

Fig. 1(b) showed the computational domain of the film cooling configuration with a single row of round holes in the target plate. The computational domain consisted of three sub-zones, namely the mainstream flow zone, coolant flow zone and solid zone. The target flat plate was equipped with a single row of large cylindrical holes with diameter of 12.7 mm (D) inclined at 35° and fed with the coolant from a plenum at a constant pressure. The original point of the global coordination was the center point of the film cooling hole on the exit surface. The domain extended 18D upstream and 30D downstream from the original point. The size of the mainstream domain was 3D × 10D × 48D (width × height × length) and the size of the coolant path was 3D × 5D × 48D (width × height × length). The thickness of the plate was 1.8D, and the distances between the center of the film holes and the two periodic planes were both 1.5D.

To investigate the influence of the inclined angle of the PDTC on the cooling effectiveness, the parameters, α and β, were defined as inclined angles between the X axis (global coordination) and ζ axis (local coordination) on the X-Z plane and X-Y plane, respectively, as shown in Fig. 1(c). The two angles varied from 0° to 90° in the simulations.

2.2. Governing equations

The study used a general purpose CFD code, ANSYS FLUENT v14.0, which is based on the finite volume method. The mass, momentum and energy governing equations of a compressible ideal gas in steady state can be described as [33]:

$$\frac{\partial \rho \overline{u_i}}{\partial x_i} = 0 \tag{1}$$

$$\rho \overline{u}_j \frac{\partial \overline{u}_i}{\partial x_j} = \rho \overline{F}_i - \frac{\partial \overline{p}}{\partial x_i} + \frac{\partial}{\partial x_j}\left[\mu\left(\frac{\partial \overline{u}_i}{\partial x_j} + \frac{\partial \overline{u}_j}{\partial x_i}\right) - \rho \overline{u_i' u_j'}\right] \tag{2}$$

$$\rho \overline{u}_j \frac{\partial \overline{T}}{\partial x_j} = \frac{\partial}{\partial x_j}\left(\frac{\lambda}{c_p}\frac{\partial \overline{T}}{\partial x_j} - \rho \overline{u_j' T'}\right) \tag{3}$$

where the over bars denote the mean values, and $\overline{F}_i$ stands for the body force. The term $-\rho \overline{u_i' u_j'}$ is the Reynolds stress tensor and $-\rho \overline{u_i' T'}$ the turbulent heat flux, which can be modeled as shown in Eqs. (4) and (5) based on the Boussinesq eddy-viscosity assumption:

$$-\rho \overline{u_i' u_j'} = \mu_t\left(\frac{\partial \overline{u}_j}{\partial x_i} + \frac{\partial \overline{u}_i}{\partial x_j}\right) - \frac{2}{3}\rho k \delta_{ij} \tag{4}$$

$$-\rho \overline{u_i' T'} = \frac{\mu_t}{Pr_t}\frac{\partial \overline{T}}{\partial x_i} \tag{5}$$

A realizable k-ε turbulence model was used to model turbulence in the present study, since it has been successfully applied to study the conjugated heat transfer and film cooling effectiveness in previous studies [34–36].

The transport equations for the turbulent kinetic energy (k) and its dissipation rate (ε) are described as [37]:

$$\frac{\partial}{\partial x_j}(\rho k u_j) = \frac{\partial}{\partial x_j}\left[\left(\mu + \frac{\mu_t}{\sigma_k}\right)\frac{\partial k}{\partial x_j}\right] + G_k + G_b - \rho\varepsilon - Y_M + S_k \tag{6}$$

$$\frac{\partial}{\partial x_j}(\rho \varepsilon u_j) = \frac{\partial}{\partial x_j}\left[\left(\mu + \frac{\mu_t}{\sigma_\varepsilon}\right)\frac{\partial \varepsilon}{\partial x_j}\right] + \rho C_1 S_\varepsilon - \rho C_2 \frac{\varepsilon^2}{k + \sqrt{\nu\varepsilon}} + C_{1\varepsilon}\frac{\varepsilon}{k} C_{3\varepsilon} G_b + S_\varepsilon \tag{7}$$

where G_k represents the generation of turbulence kinetic energy due to the mean velocity gradients, G_b is the generation of turbulence kinetic energy due to buoyancy, and Y_M represents the contribution of the fluctuating dilatation in compressible turbulence to the overall dissipation rate. S_k and S_ε are user-defined source terms. The eddy viscosity μ_t is calculated as:

$$\mu_t = \rho C_\mu \frac{k^2}{\varepsilon} \tag{8}$$

And the model constants are:

$$C_{1\varepsilon} = 1.44, C_2 = 1.9, \sigma_k = 1.0, \sigma_\varepsilon = 1.2 \tag{9}$$

The Enhanced Wall Treatment (EWT) was applied in the near-wall region. That is, the two-equation k-ε model was employed in the fully-turbulent region, and the one-equation model of Wolfstein was employed in the viscosity-affected near-wall region [38].

In the solid region, the traditional universal energy transport equation has the following form [37]:

$$\frac{\partial \rho \overline{v}_j h}{\partial x_j} = \frac{\partial}{\partial x_j}\left(k_{ij}\frac{\partial T}{\partial x_j}\right) + S_h \tag{10}$$

where h is the sensible enthalpy, S_h is the volumetric heat source, and k_{ij} is the thermal conductivity which is anisotropic in this paper. The term on the left-hand side represents convective energy transfer due to rotational or translational motion of the solids. The velocity field $\overline{v_j}$ is computed from the motion specified for the solid zone. In this paper this term is zero because the solid region is stationary.

According to the study in Ref. [39], the heat flux vector with anisotropic heat conduction may be written as:

$$q_i = -k_{ij}\frac{\partial \overline{T}}{\partial x_j} \tag{11}$$

where k_{ij} is the matrix of the anisotropic thermal conductivity.

In general, k_{ij} can be expressed as:

$$k_{ij} = \begin{bmatrix} k_{XX} & k_{XY} & k_{XZ} \\ k_{YX} & k_{YY} & k_{YZ} \\ k_{ZX} & k_{ZY} & k_{ZZ} \end{bmatrix} \tag{12}$$

Eq. (12) can be rewritten as below:

$$\begin{bmatrix} k_{XX} & k_{XY} & k_{XZ} \\ k_{YX} & k_{YY} & k_{YZ} \\ k_{ZX} & k_{ZY} & k_{ZZ} \end{bmatrix} = \begin{bmatrix} l_1 & m_1 & n_1 \\ l_2 & m_2 & n_2 \\ l_3 & m_3 & n_3 \end{bmatrix} \begin{bmatrix} k_\xi & 0 & 0 \\ 0 & k_\eta & 0 \\ 0 & 0 & k_\nu \end{bmatrix} \begin{bmatrix} l_1 & l_2 & l_3 \\ m_1 & m_2 & m_3 \\ n_1 & n_2 & n_3 \end{bmatrix} \tag{13}$$

where

$$\begin{bmatrix} l_1 & m_1 & n_1 \\ l_2 & m_2 & n_2 \\ l_3 & m_3 & n_3 \end{bmatrix} = \begin{bmatrix} \cos\gamma\cos\beta & -\cos\alpha\sin\gamma + \cos\gamma\sin\beta\sin\alpha & \sin\gamma\sin\alpha + \cos\gamma\sin\beta\cos\alpha \\ \sin\gamma\cos\alpha & \cos\gamma\cos\alpha + \sin\gamma\sin\beta\sin\alpha & -\cos\gamma\sin\alpha + \sin\gamma\sin\beta\cos\alpha \\ -\sin\beta & \cos\beta\sin\alpha & \cos\beta\cos\alpha \end{bmatrix} \tag{14}$$

Eq. (14) shows the transform matrix between the local coordinate (principal direction of the thermal conductivity) and the global Cartesian coordinate with the inclined PDTC angles α, β and γ. Note that γ always remains zero in the present study.

The thermal conductivity at different parts of solid can be calculated according to Eqs. (13) and (14). Then the matrix k_{ij} can be obtained. In the numerical simulations, the thermal conductivity of each element was given according to k_{ij}. The temperature field was calculated with these anisotropic thermal conductivities by finite volume method.

2.3. Boundary conditions and parameter definitions

The boundary conditions in the present simulations were specified as follows (also summarized in Table 1):

- The mainstream passage: the mainstream inlet was given a constant velocity, i.e. u_∞ = 20 m/s, with a constant total temperature of 600 K and a turbulence intensity of 0.2%. At the outlet, the pressure-outlet condition was applied with a static pressure of p_{out} = 101,325 Pa.
- The coolant plenum: the coolant jet was introduced in the lower confined flow zone. A constant mass flow flux was imposed at the inlet, with a value of 0.001463 kg/s. This value was determined according to a blowing ratio (Br) of 0.5. The total temperature at the inlet was set to be 306 K. Moreover, to investigate the effects of Br, the Br was varied from 0.5 to 1.5 in the simulations, and was defined as

Table 1
Boundary conditions.

Mainstream passage	Velocity-inlet	20 m/s
	Temperature	600 K
	Turbulence intensity	0.2%
	Pressure-outlet	101,325 Pa
Coolant plenum	Br	0.5, 1.0, 1.5
	Temperature	306 K

$$Br = \frac{\rho_c u_c}{\rho_\infty u_\infty} \tag{15}$$

where ρ_∞ and u_∞ are density and velocity of mainstream at the mainstream inlet, respectively, ρ_c and u_c are density and velocity of the coolant flow at the inlet of film hole, respectively.

Consistent with previous studies, we used the adiabatic cooling effectiveness (η_{aw}) and the overall cooling effectiveness (η) to represent the film cooling performance, which are defined in Eqs. (16) and (17), respectively:

$$\eta_{aw} = \frac{T_\infty - T_{aw}}{T_\infty - T_c} \tag{16}$$

$$\eta = \frac{T_\infty - T_w}{T_\infty - T_c} \tag{17}$$

where T_∞ is the mainstream inlet temperature, T_c the coolant inlet temperature, T_{aw} the adiabatic temperature of the hot-side wall and T_w the temperature of the hot-side wall in the conjugated heat transfer case.

The average cooling effectiveness is defined as Eq. (18):

$$\bar{\eta} = \frac{T_\infty - \overline{T}_w}{T_\infty - T_c} \tag{18}$$

where $\overline{T}_W$ is the average wall temperature.

The standard deviation of cooling effectiveness, denoted as σ, was introduced to describe the uniformity of the cooling effect on the wall:

$$\sigma = \sqrt{\frac{1}{N}\sum_{i=1}^{N}(\eta_i - \bar{\eta})^2} \tag{19}$$

where η_i and $\bar{\eta}$ are the local cooling effectiveness and average cooling effectiveness, respectively.

In this study, the primary interests are the cooling effects on the hot-side wall and in the middle section of the film cooling plate. Two additional specific lines and three specific regions were introduced (as shown in Fig. 2) in order to demonstrate the results of film cooling performance more clearly.

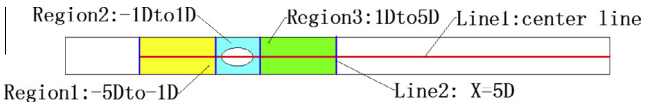

Fig. 2. Schematic diagram of specific lines and flow regions.

Table 2
Summary of cases studied.

Case	$k_\zeta/k_\eta/k_\nu$ (W/(m K))	Inclined angle	$k_{XX}/k_{YY}/k_{ZZ}$ (W/(m K))
1	Adiabatic	–	Adiabatic
2	0.455/0.455/0.455	–	0.455/0.455/0.455
3	1.82/0.455/0.455	α = 0°, β = 0°	1.82/0.455/0.455
4	1.82/0.455/0.455	α = 30°, β = 0°	1.479/0.455/0.796
5	1.82/0.455/0.455	α = 35°, β = 0°	1.37/0.455/0.91
6	1.82/0.455/0.455	α = 60°, β = 0°	0.796/0.455/1.479
7	1.82/0.455/0.455	α = 90°, β = 0°	0.455/0.455/1.82
8	1.82/0.455/0.455	α = 0°, β = 30°	1.479/0.796/0.455
9	1.82/0.455/0.455	α = 0°, β = 60°	0.796/1.479/0.455
10	1.82/0.455/0.455	α = 0°, β = 90°	0.455/1.82/0.455

We performed ten flow cases with different values of α and β in order to study the effects of the inclined angles of PDTC, and these results are summarized in Table 2. Case 1 examined the adiabatic cooling effectiveness, Case 2 studied the overall cooling effectiveness in plates with the isotropic thermal property, and Cases 3–10 represent the elucidation of the overall cooling effectiveness in anisotropic plates with different inclined PDTC angles.

A homogeneous material with a thermal conductivity of 0.455 W/(m K) was used in the isotropic case, while k_ζ, kη and kν were specified the values of 1.82 W/(m K), 0.455 W/(m K) and 0.455 W/(m K), respectively, for the anisotropic cases. These effective thermal conductivities were chosen according to the in-house measured data of a typical carbon long fiber reinforced composite (FRC). This composite consisted of an epoxy-resin matrix and continuous aligned T300 carbon long fiber. The average volume ratio of this carbon FRC was 65%, which is defined as the ratio of the fibers' volume to the composite's volume. A NETZSCH LFA 457 Micro-Flash instrument was used to elucidate the thermal diffusion coefficient. The specific heat capacity was measured with a DSC 200 F3, and the equivalent thermal conductivity was calculated with the thermal diffusivity and specific heat capacity. As mentioned above, the experiment by Mutnuri [23] and the study by Tian [24] indicated that the effective thermal conductivity of a typical carbon/vinyl ester composite and typical carbon-fiber/epoxy composite are around 1.035 W/m K to 6.316 W/m K (along the longitudinal direction), 0.611 W/m K (transverse direction), respectively. In this paper, 1.82 W/(m K), 0.455 W/(m K) and 0.455 W/(m K) were used as the effective thermal conductivities in the anisotropic cases, which reflect the data from published literatures.

The inclined angles and corresponding thermal conductivities on the X, Y and Z axis (k_{XX}, k_{YY} and k_{ZZ}) are shown in Table 2 for all the 10 cases applied in the present study.

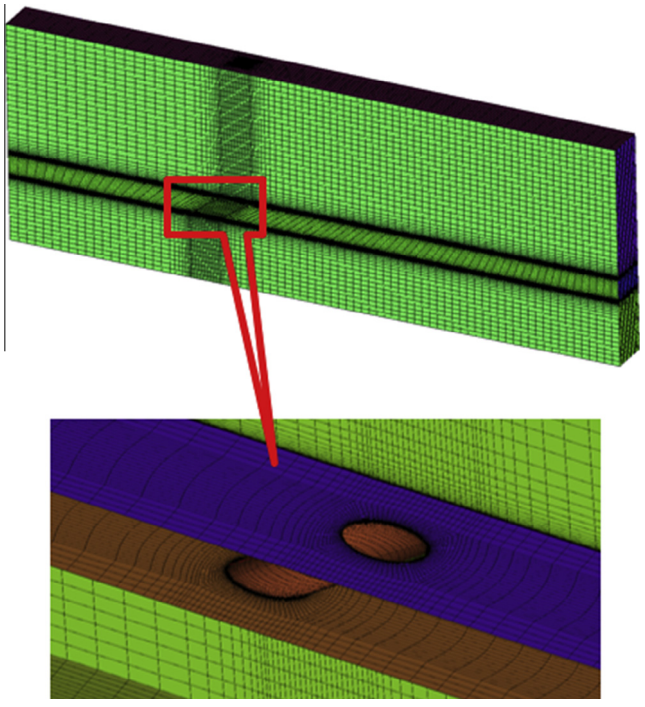

Fig. 3. Computational grids.

2.4. Grid system

We used a hexahedral grid in this study, shown in Fig. 3. In the near-wall region, the mesh was refined in order to accurately capture the steep gradients of pressure, velocity and temperature. The dimensionless distance y^+ of the first mesh center to the wall was smaller than 1 with respect to the criteria required for the individual near-wall treatment. The mesh was stretched away from the viscous wall with a stretching ratio less than 1.2.

The grid dependency test was carried out with the total number of grids changing from 95,992 to 1,000,896, by which the first height of grid was constant and the stretching ratio of grid was decreased by 10% per time. Fig. 4 shows the influence of the grid number on the cooling effectiveness of Line 1 and Line 2 (as shown

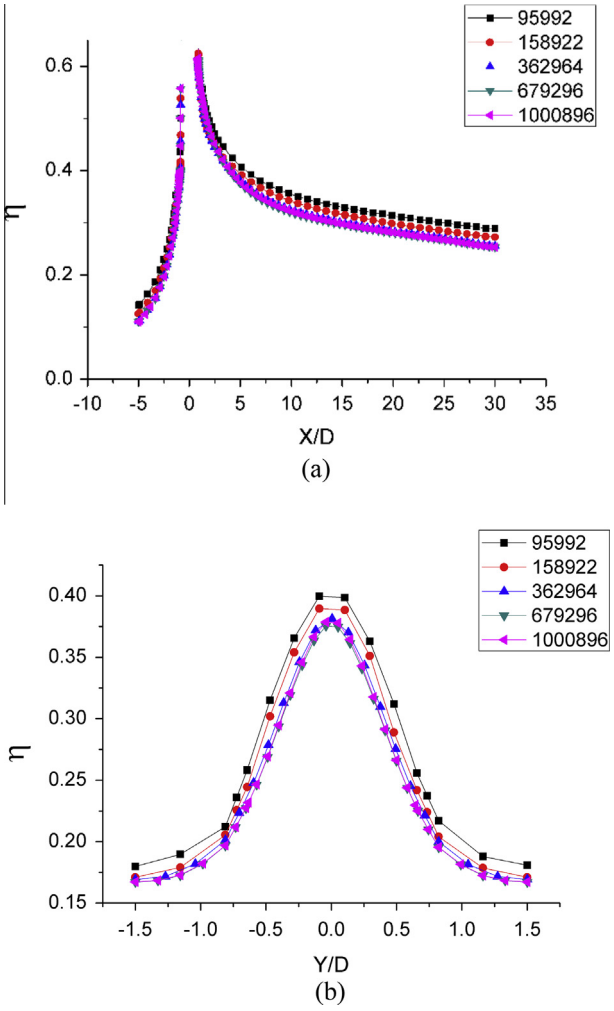

Fig. 4. Comparison between numerical results with different meshs at two locations: (a) Line 1 and (b) Line 2.

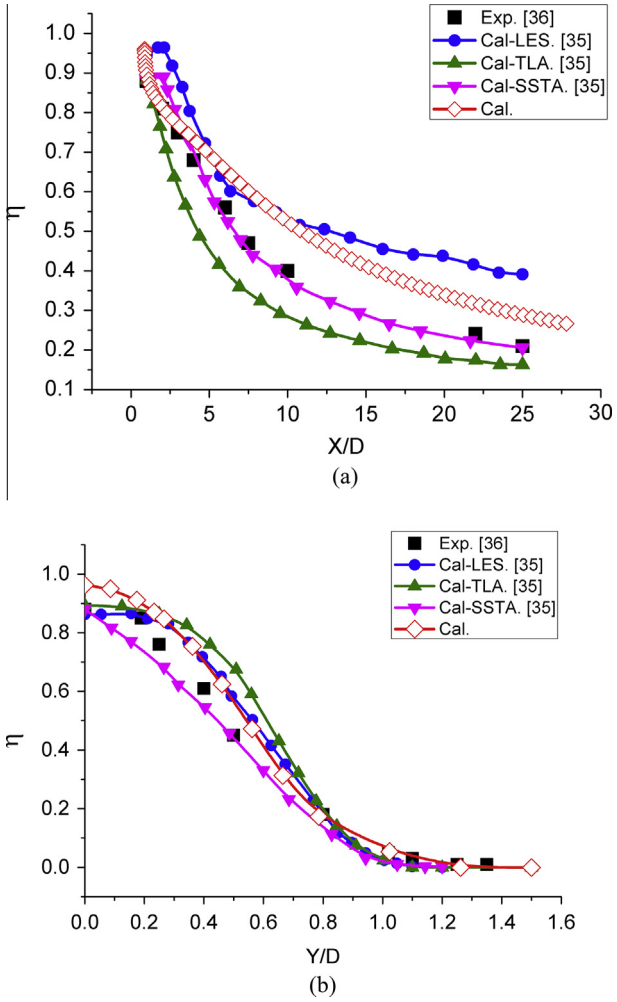

Fig. 5. Comparison of the present numerical predictions and experimental results at two locations: (a) central line and (b) X/D = 1.

in Fig. 2). The criterion of grid independence is that the average fluctuation is smaller than 3%. The result shows that the cooling effectiveness is not sensitive to the grid number when it is more than 679,296. Therefore, the grid with 679,296 nodes was selected for the computations, which has $110 \times 30 \times 45$ nodes in the X, Y and Z directions of the mainstream section duct.

3. Results and discussions

3.1. Validation of the computational method

The present numerical method was first applied to a case previously studied by Bianchini et al. [40] in order to validate the present simulation code. Comparison between the present numerical results, the previous numerical data [40] and the experimental data [41] is shown in Fig. 5 for the adiabatic cooling effectiveness at two locations of the centerline and the span-wise line (X/D = 1).

Comparisons in Fig. 5 demonstrate that the predictions agree reasonably well with the experimental data. The adiabatic cooling effectiveness was well predicted at the location of the central line, although it was slightly overestimated in the far downstream region (X/D > 10). The numerical results at the location in the span-wise direction (X/D = 1) also show good agreement with the experimental data. The average relative error was about 10.97%, which is comparable to the relative error of the numerical results in Ref. [40].

The results in Fig. 5 demonstrate that the adiabatic cooling effectiveness decreased significantly along the streamwise direction. It decreased down to nearly 50%, when it extended to the 10D downstream location. This observation is consistent with the experimental results in Ref. [41].

3.2. Comparison of adiabatic, isotropic and typical anisotropic cases

Fig. 6 presents the temperature distributions at the hot-side wall and in the middle section from Cases 1, 2 and 7. (Note that there is no middle-section in Case 1 because it only has a thin slice.)

There are significant differences between the results for the three cases, especially between Case 1, Case 2 and Case 7. The

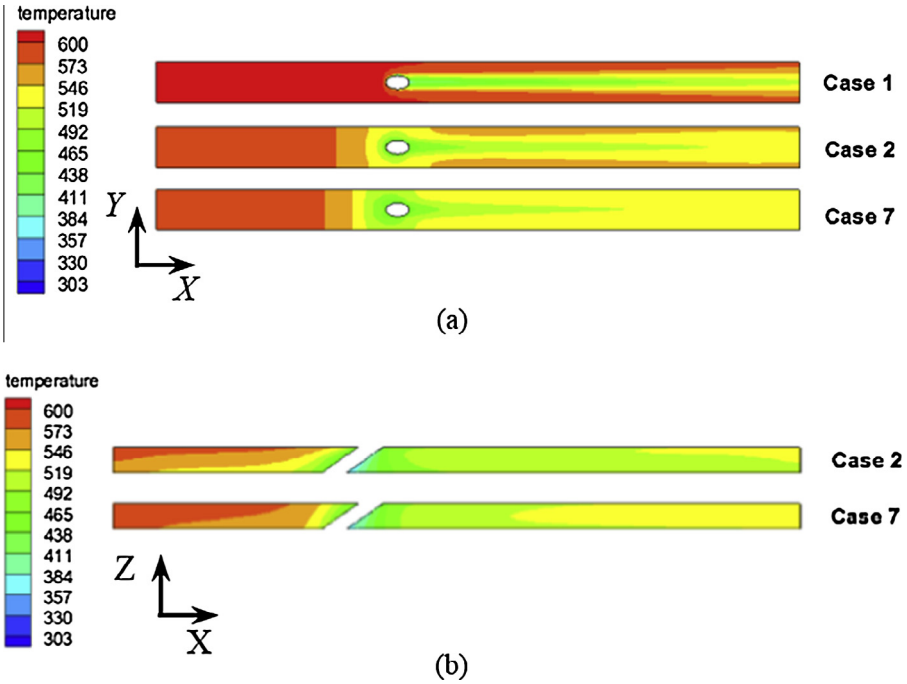

Fig. 6. Temperature distributions at the hot-side-wall (a) and in the middle section (b), in Cases 1, 2 and 7.

effects of heat conduction in the solid region can be clearly observed. These results show that the mean temperature over the hot-side wall is 570.05 K, 548.80 K and 543.33 K, respectively, for Cases 1, 2 and 7.

The temperature along the hot-side wall is almost equal to the inlet temperature of the mainstream until the location where the coolant flows out, due to the adiabatic boundary in Case 1. The lower temperature mainly exists in the downstream region of the film hole.

In Cases 2 and 7, heat is transferred between the hot mainstream and the coolant via both convection and conduction. Significant temperature gradient can thus be found in these two cases, not only at the downstream region of film hole, but also at the upstream region, as shown in Fig. 6(a). Before the coolant flows out from the film hole, it may be heated by conduction, resulting in a heat transfer through the internal surfaces of the film hole. Fig. 6(b) indicates that the temperature decreases gradually in the solid region near the film hole.

Fig. 7 provides a detailed comparison between the results of Cases 2 and 7, which shows the contour plots of the cooling effectiveness in three specific local regions (1–3, as defined in Fig. 2). The cooling effectiveness for Case 2 is larger than that in Case 7 in the upstream region and very near regions of the film hole. This is because the ETC on the Z axis direction in Case 7 is larger than that in Case 2, and they have the same values in the other two directions. Correspondingly, it leads to the enhancement of the heat conduction between the hot-side wall and the coolant-side wall. The hot-side wall can thus be further cooled, resulting in a larger cooling effectiveness.

The square region marked with red[1] lines shown in Fig. 7(a) is significant. The higher cooling effectiveness can be clearly observed in this region in Case 7. Due to the inclined angle of the film hole, the thickness of the plate in this region becomes gradually smaller and the heat transfer enhancement induced by the larger thermal conductivity becomes more significant. Therefore, much higher cooling effectiveness was achieved at this region in Case 7 than that in Case 2.

Fig. 7(c) illustrates the comparison of the cooling effectiveness at region 3 for Cases 2 and 7. In the central part ($|Y| \leqslant 0.5D$), Case 2 presents a higher cooling effectiveness, while at the two side parts ($|Y| \geqslant 0.5D$), Case 7 shows a better cooling effect. This superior cooling probably resulted from the complex effects of the film cooling flow fields and the corresponding heat transfer between the mixed stream and solid surface.

To explain the phenomena more clearly, the isothermals and temperature contours at the plane of X/D = 2.5 are presented in Fig. 8. This figure shows that the temperature of the mixed fluids is higher than that in the solid region in the two side parts. The heat was thus transferred from the fluid to the solid. In the central part, the solid region has a higher temperature compared with the incomplete mixed coolant/mainstream fluids, resulting in the heat transfer in the opposite direction. Those phenomena have also been reported in the study by Ai and Fletcher [19]. However, it is more remarkable in the present study that k_{ZZ} of the solid material is almost 4 times bigger than k_{XX} and k_{YY} in Case 7.

Therefore, in the two side parts, more heat was transferred through the solid region and absorbed by the cold air in the coolant plenum, which led to a lower temperature at the hot-side surface. Similarly, in the central part, more heat was transferred from the solid region and absorbed by the coolant film. Fig. 8 shows that the isothermals are significantly curved in Case 7, indicating the variation in the heat flux direction, especially inside the solid region. Those complex heat transfers resulted in a higher cooling

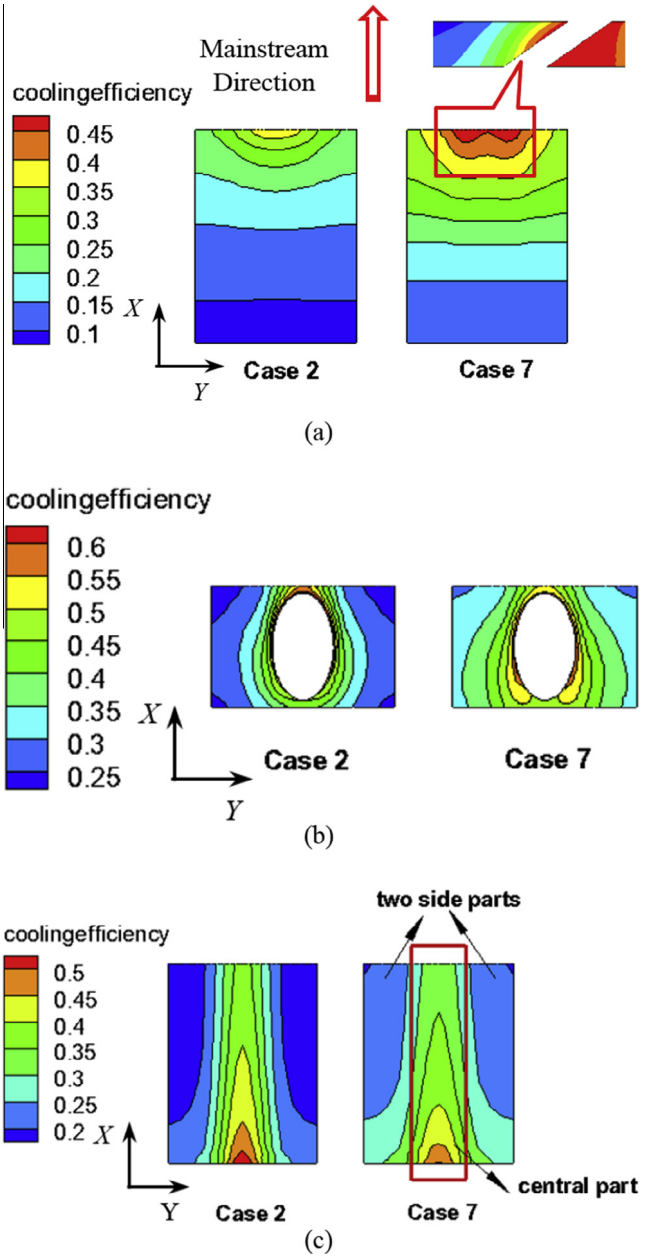

Fig. 7. Cooling effectiveness distribution in specific regions: (a) Region 1; (b) Region 2; (c) Region 3, in Cases 2 and 7.

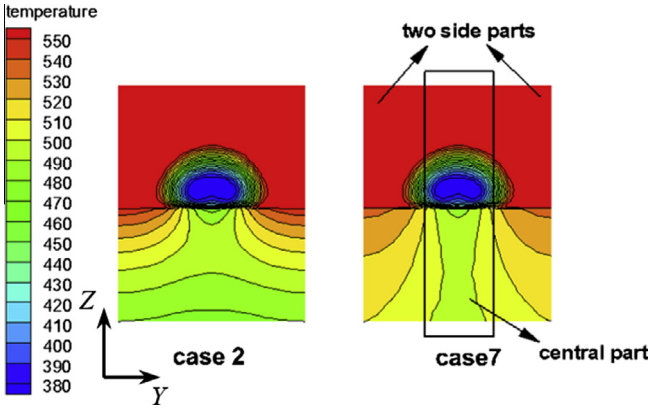

Fig. 8. Temperature distribution on the plane of X/D = 2.5 downstream the film hole in Cases 2 and 7.

[1] For interpretation of color in Figs. 7 and 13, the reader is referred to the web version of this article.

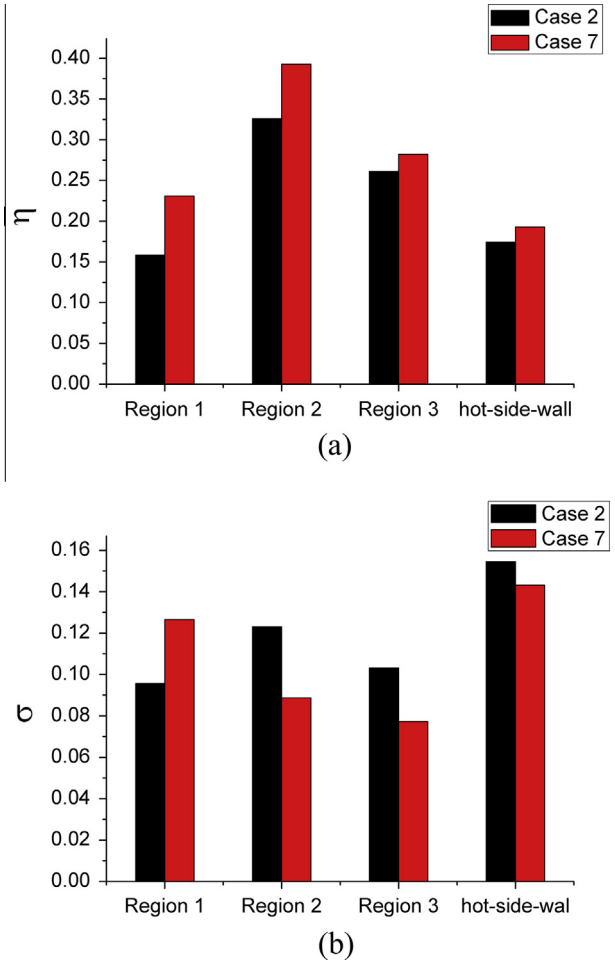

Fig. 9. The average cooling effectiveness (a) and its standard deviation (b) in three specific regions and the whole hot-side wall.

effectiveness for the two side parts and a lower cooling effectiveness in the central part in Case 7.

Fig. 9 shows the average value and the standard deviation of the cooling effectiveness over the three local regions (regions 1, 2, 3) and the whole area of the hot-side wall. Case 7 produced a higher average cooling effectiveness in all the regions of interests. A lower standard deviation of the cooling effectiveness was found in regions 2 and 3 in Case 7, while it was higher in region 1 in Case 7. Those variations in the standard deviation indicated that more uniform cooling effects were achieved in Case 7 for most of the regions, except region 1. This finding can be attributed to the anisotropic thermal conductivities.

3.3. Effect of the angle α

Fig. 10 shows the temperature distributions on the hot-side wall and in the middle section with α varying from 0° to 90°, with β remains 0°. The temperature distributions changed on the two planes, especially in the middle section. With increasing α, it resulted in a smaller hot area on the hot-side wall, but a larger hot area in the middle section.

According to Eqs. (11)–(14), the vertical component of the thermal conductivity, k_{ZZ}, is determined to be 0.455, 0.796, 0.91, 1.479 and 1.82 W/(m K), respectively, with the inclined angle α increasing from 0° to 90°. The heat transfer could thus be enhanced in the Z direction, as discussed above. Correspondingly, the area of the lower temperature region on the hot-side wall becomes larger with increasing α, and the temperature in the region near the coolant plenum becomes higher, as shown in Fig. 10(b). The horizontal component of the thermal conductivity, k_{XX}, also changed with varying α. Thus, a larger temperature gradient in the solid region in the X direction was observed in the middle section.

Fig. 11 shows the distributions of the cooling effectiveness in three specific local regions with α increasing from 0° to 90°. Fig. 11(a) and (b) shows that the cooling effectiveness improved significantly with increasing α, especially in regions 1 and 2. In the downstream region 3, the cooling effectiveness in the two-

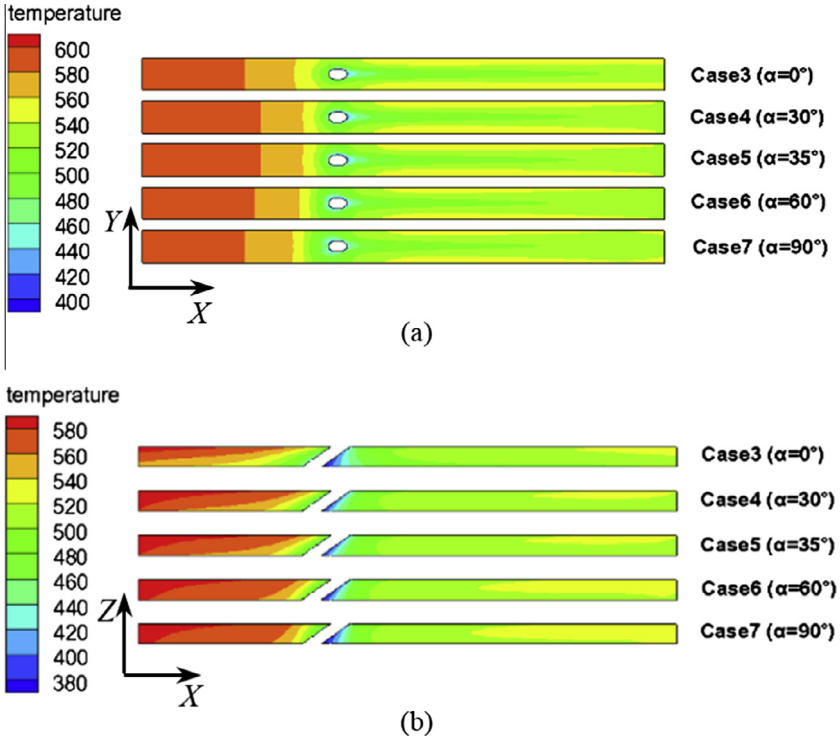

Fig. 10. Temperature distribution on the hot-side wall (a) and in the middle section (b), with varying α.

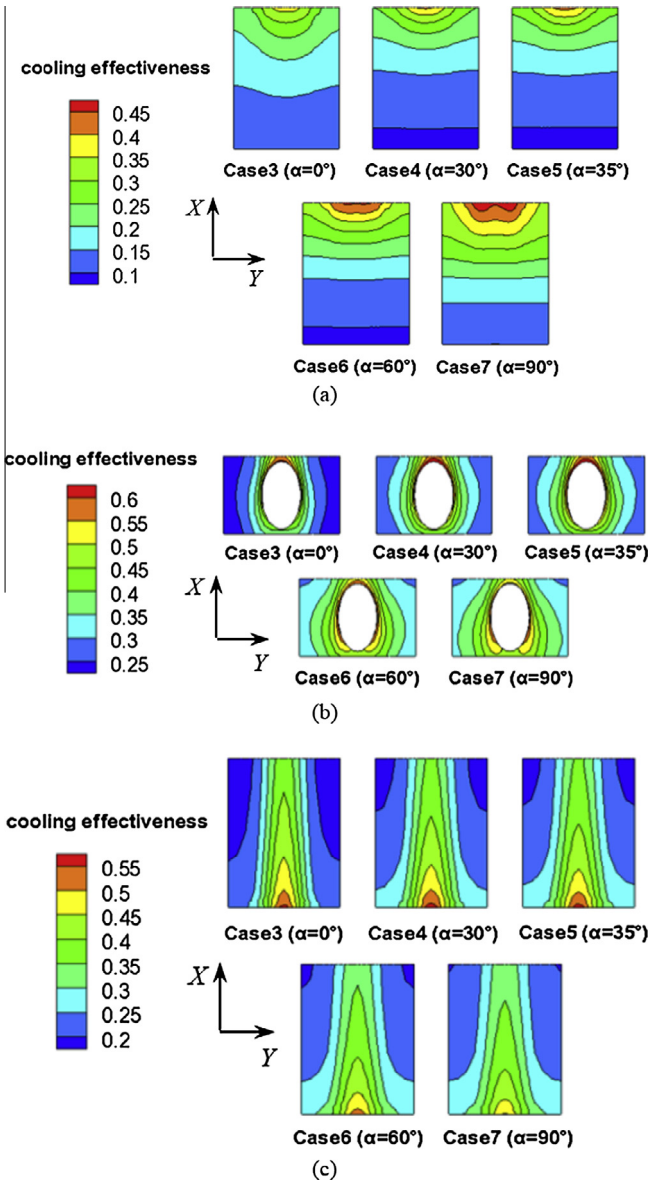

Fig. 11. Cooling effectiveness distribution in specific regions: (a) Reion 1; (b) Region 2; (3) Region 3, with increasing α.

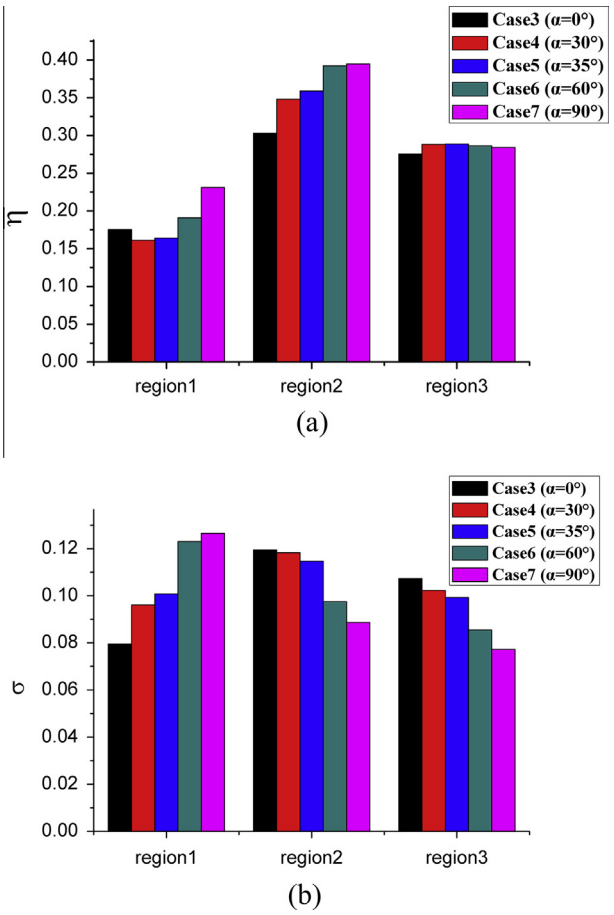

Fig. 12. The average cooling effectiveness (a) and its standard deviation (b), in three specific regions with increasing α.

side part was enhanced, while the cooling effect was somewhat weakened in the central part. The reason for this phenomenon is the same as discussed in Section 3.2. It is shown in Fig. 8 that is the variation of the vertical component of thermal conductivity k_{zz} affects the heat transfer in the solid region.

To further elaborate on the effects of the inclined angle α, Fig. 12 presents the average cooling effectiveness ($\overline{\eta}$) and its standard deviation (σ) in three local regions. A higher $\overline{\eta}$ and smaller σ were observed with a larger α generally, except in region 1. Taking Case 7 and Case 4 as examples, $\overline{\eta}$ was increased by 13% and σ reduced by 25% in region 2. However, in region 1, σ was increased by nearly 40%, while $\overline{\eta}$ increased only about 7%. This is mainly due to the significantly high cooling effectiveness in the region of the leading edge of the film hole, as shown in Fig. 11(a), where the wall thickness of the plate was small and the thermal conductivity was higher in the z direction with a larger α.

The parameter $\overline{\eta}$ in region 3 (Fig. 12(a)) almost retained the same value in all the cases with different values of α. However, the standard deviation (σ) was significantly lower – decreased by about 38%, comparing Case 7 and Case 4. It is because that the vertical heat conduction in the solid was enhanced with increasing α. There was a relative reduction in the horizontal heat conduction, especially between the region near the side surface of the film hole and the region far away from the film hole. The heat transfer was weakened from the solid region to the coolant through the side surfaces of the film hole. As it was affected by the two comparative processes, $\overline{\eta}$ in region 3 thus retained almost the same value.

Here, we discuss the local heat flux in region 3 in more details to reveal the complex interactions. Fig. 13(a) presents the contour of the heat flux, in which a positive value stands for the heat transfer from the mixed stream to the solid, while a negative value represents the opposite process. It can be seen that, in the central region, the heat was transferred from the solid region to the fluid region, marked with red lines in Fig. 13(a). However, heat was transferred from the mixed mainstream to the solid in the other regions.

Fig. 13(b) shows the dependence of the average absolute heat flux variance with α through the central region. The result shows that the absolute heat flux increased with increasing α, indicating that more heat was transferred into the mixed mainstream through the central part with increasing α.

Those results demonstrated a weakened cooling effectiveness in the central region and an enhanced cooling effectiveness in other regions. The value of $\overline{\eta}$ barely changed in region 3, but the cooling effect was more uniform with increasing α in region 3 during the same time, as shown in Fig. 12(b).

3.4. Effect of the angle β

Fig. 14 shows the temperature distributions at the hot-side wall and in the middle section with increasing β from 0° to 90°, while α

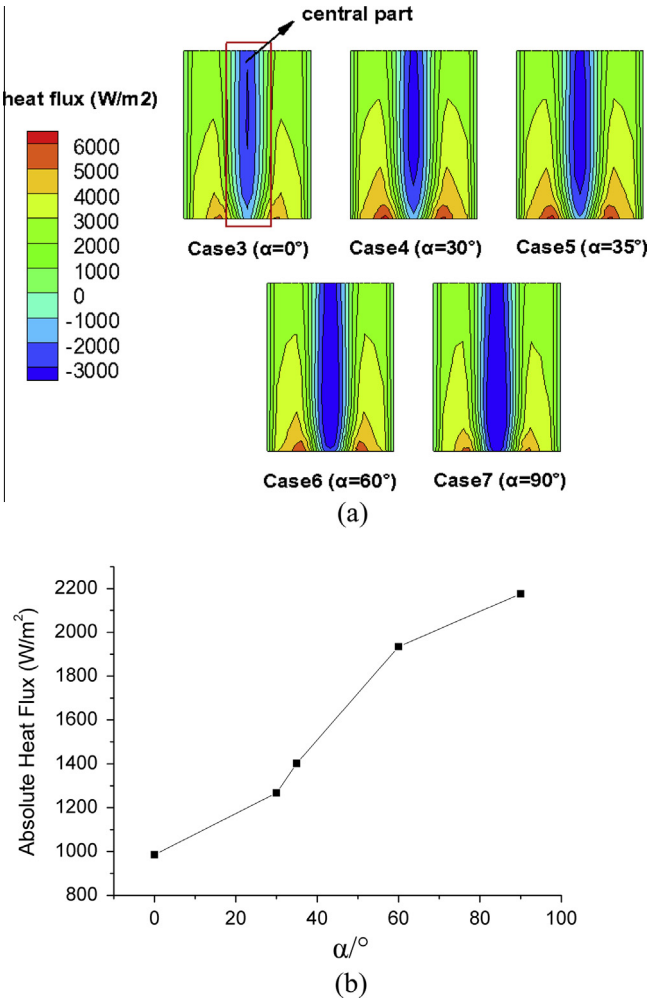

Fig. 13. Heat flux distribution in Region 3 (a) and the average absolute heat flux in central part with increasing α (b).

remains 0°. The results show that the temperature distributions on the hot-side wall and in the middle section slightly change with increasing β, except in the regions very close to the film holes.

According to Eqs. (11)–(14), the span-wise components of the thermal conductivity, k_{XX} and k_{YY}, change, while k_{ZZ} remains the same, with varying β. The main temperature gradient in the film cooling configuration exists in the z direction and the variation of k_{XX} and k_{YY} does not significantly affect the heat transfer. The results in Fig. 14(b) clearly demonstrate this point. The distributions of the temperature are almost the same in Cases 3, 8, 9 and 10, indicating that the heat flux is weakly changed along the z direction.

More details about η in the three regions are presented in Fig. 15. In region 1, the distribution of η only changes slightly between different cases and the isolines become flatter with increasing β due to the increase of the thermal conductivity, k_{YY}. Region 2 contained a large gradient in the horizontal and span-wise directions as heat was transferred from the solid to the coolant through the side surface of the film hole. Heat transportation in this region was dominated by k_{XX} and k_{YY} and thus quite different contours of η are observed in Fig. 15(b) as β increased from 0° to 90°. The highest η was produced in the case with β = 90°. In region 3, the effects of the horizontal and span-wise heat conduction on η were weakened due to the strong heat convection between the mixed stream and the solid. The distributions of η slightly changed as shown in Fig. 15(c), although k_{XX} and k_{YY} were significantly different in different cases.

Fig. 16 shows $\overline{\eta}$ and σ in three specific regions and highlights the effects of the inclined angle β. It clearly indicates that, in all cases, $\overline{\eta}$ remains almost the same, except in region 2. A larger β results in a better uniformity of film cooling, except in region 1.

3.5. Influence on different downstream regions with different blowing ratios

From the discussions above, it can be concluded that the effects of the inclined angles of PDTC on the cooling effectiveness are different for each flow region. In engineering applications, the downstream region of the film cooling is generally of more interests, as it is the target region protected by film cooling. Therefore,

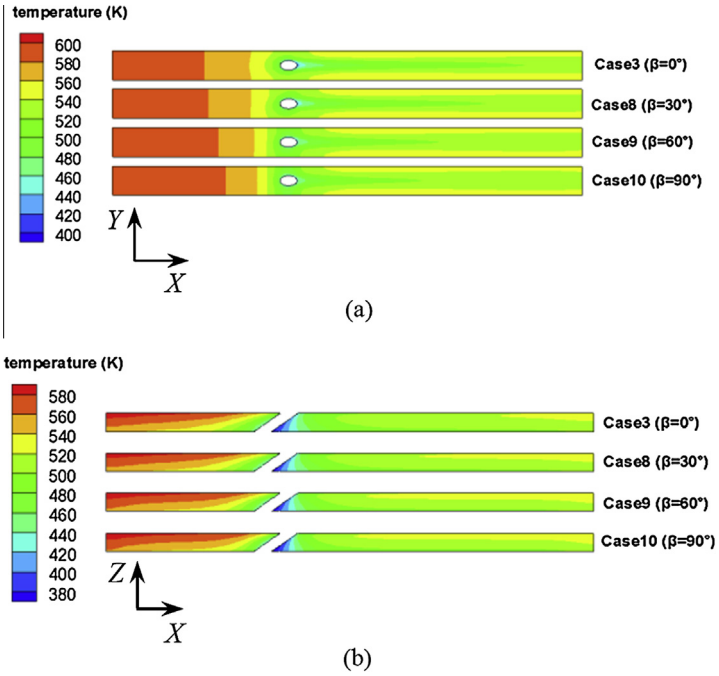

Fig. 14. Temperature distribution at the hot-side wall (a) and in the middle section (b), with increasing β.

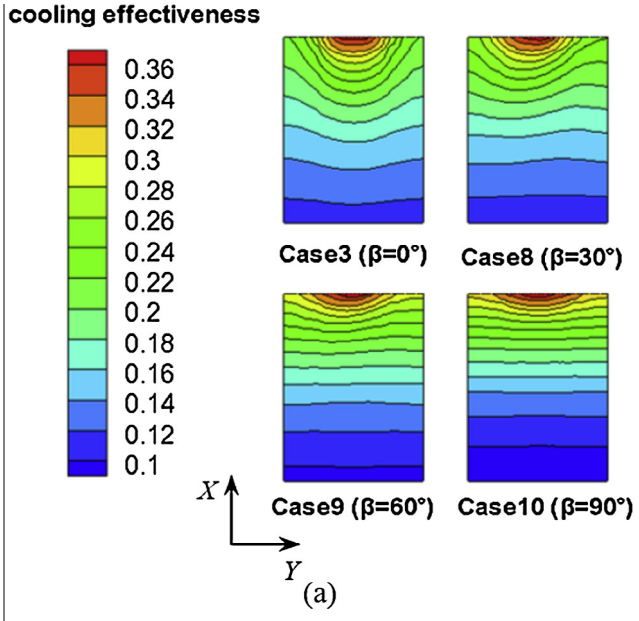

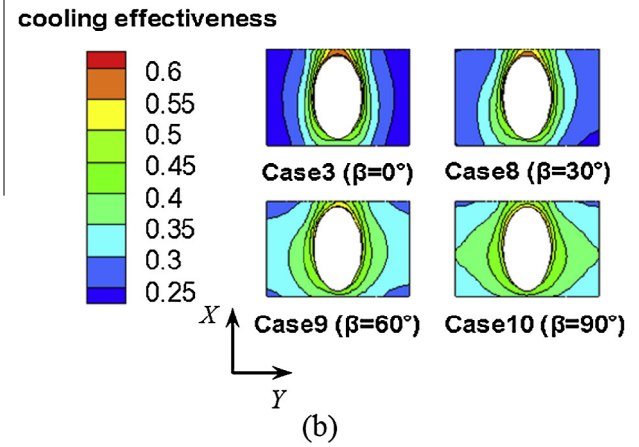

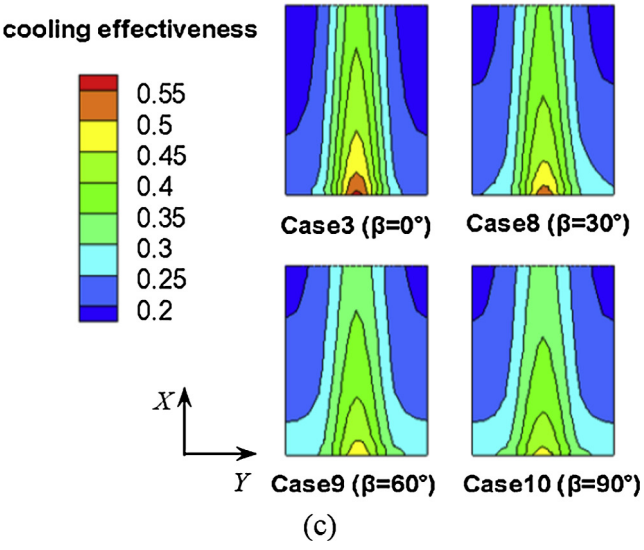

Fig. 15. Cooling effectiveness distribution in three specific regions: (a) Region 1; (b) Region 2; (c) Region 3, with increasing β.

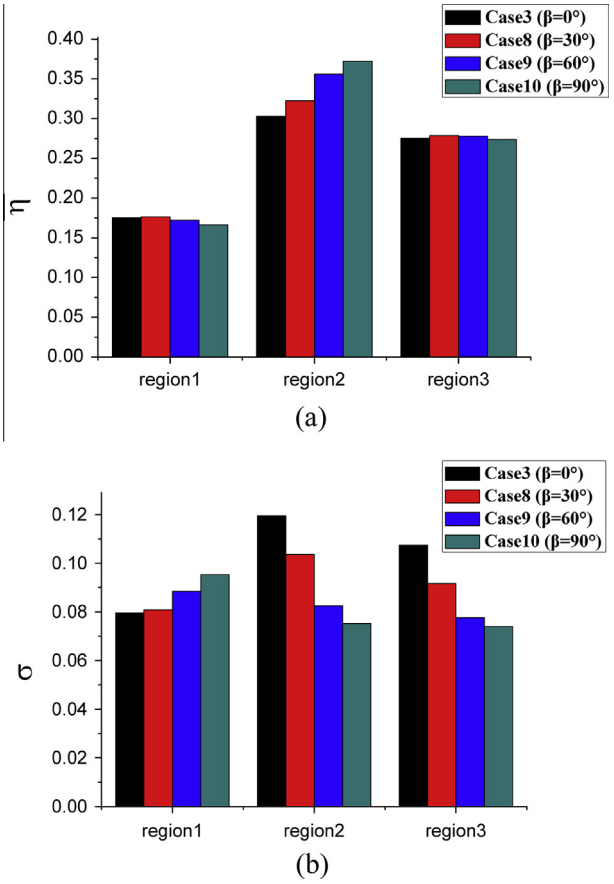

Fig. 16. The average cooling effectiveness (a) and its standard deviation (b) in three specific regions with increasing β.

a detailed analysis of the inclined angle effects in this region was elucidated in this section. Four additional specific downstream regions of film cooling were defined in Fig. 17(a), and are referred to as regions 0–3D, 0–5D, 0–10D and 0–20D, respectively. Furthermore, the effects of the inclined angles with different blowing ratios are also investigated in this section.

Fig. 17(b)–(g) shows $\overline{\eta}$ and σ in those different regions with varying α and β under different blowing ratios. The effects of the inclined angle when the blowing ratio equals 0.5 are given in Fig. 17(b) and (c). Fig. 17(b) shows that, compared with the inclined angle α, angle β affects $\overline{\eta}$ much more weakly. It results that $\overline{\eta}$ -β curves are much flatter than the $\overline{\eta}$ -α curves. The highest value for $\overline{\eta}$ depended on the angle and downstream region of interests. For example, α should be around 35° in order to produce the highest $\overline{\eta}$ if 0–5D region is the object, while the value changes to around 90° when 0–20D region is the focus. Fig. 17(c) also shows that σ decreases with increasing β, and it is not monotonically affected by α. The best uniformity in the film cooling effect was obtained when β approaching 90°.

All the results above are obtained under the condition that Br has a value of 0.5. Fig. 17(d)–(g) shows the variations of $\overline{\eta}$ and σ with Br = 1.0 and Br = 1.5. It can be found that the effects of α and β on $\overline{\eta}$ are similar with different Br. The highest $\overline{\eta}$ is obtained when α is around 35° if 0–5D region is chosen as the object, while this value changes to around 90° when 0–20D region is the focus. However, σ is affected by α and β non-monotonically in different Br cases, especially when different regions are considered.

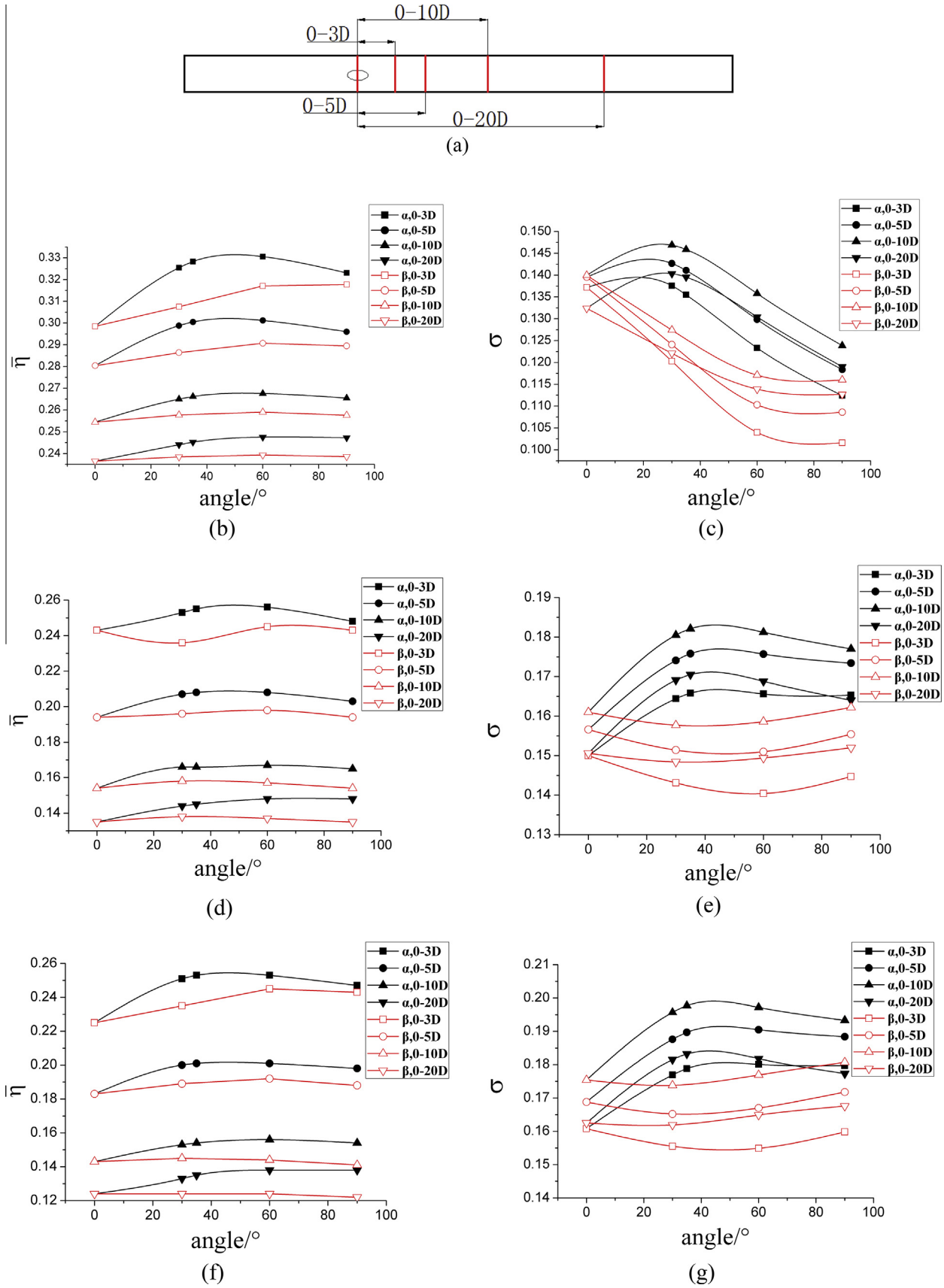

Fig. 17. Four additional specific downstream regions (a) and its average cooling effectiveness and standard deviation with Br = 0.5 ((b) and (c)), Br = 1.0 ((d) and (e)) and Br = 1.5 ((f) and (g)).

4. Conclusions

Numerical study was carried out on the film cooling from a single row of holes on a composite plate with focus on the effects of anisotropic thermal conductivity. The results of temperature, heat flux and cooling effectiveness were examined and discussed in detail. The effects of the inclined angles of the PDTC on the film cooling effectiveness were investigated. The main observations can be summarized as follows:

(1) There are significant differences in the temperature fields between the adiabatic case and the conjugated heat transfer cases. The effects of anisotropic thermal conductivities are complex which significantly affect the temperature and heat flux flow fields.
(2) Besides the effects of the discrete film holes and anisotropic thermal conductivity, the non-uniform temperature distribution was also influenced significantly by the inclined angle of the PDTC. The effects on the cooling effectiveness are complex and depend on the specific configurations of the inclined angles and thermal conductivity.
(3) The highest average cooling effectiveness can be achieved with different values of α or β when different regions downstream of the film cooling are considered. We found that, when Br equals 0.5, the axial angle α should be around 35° in order to produce the highest average cooling effectiveness with focus on the 0–5D downstream region. This value changes to 90° when the 0–20D downstream region was considered. Compared with the axial inclined angle α, the span-wise inclined angle β had a weak influence on the average cooling effectiveness at the hot-side wall. However, the uniformity of the cooling effect can be improved with larger inclined angle β.
(4) The effects of α and β on $\overline{\eta}$ are similar in different Br cases, but σ is affected by α and β non-monotonically in different Br cases, especially when different downstream regions of film holes are considered.

Acknowledgements

This work was financially supported by the National Natural Science Foundation of China (Grant No: 51606095), the Jiangsu Provincial Natural Science Foundation of China (Grant No: BK20160794). X.S. Han acknowledges the support of Jiangsu Specially-Appointed Professor Program. The authors are also grateful to the School of Material Sciences, Nanjing University of Aeronautics and Astronautics, for the use of their facilities in the performance of this work.

References

[1] C.D. Fang, Development Research of Aeroengine, Aviation Industry Press, 2009.
[2] K. Hiroshi, The application of ceramic-matrix composites to the automotive ceramic gas turbine, Compos. Sci. Technol. 59 (1999) 861–872.
[3] Y. Deng, W.G. Li, R.Z. Wang, The temperature-dependent fracture models for fiber-reinforced ceramic matrix composites, Compos. Struct. 140 (2016) 534–539.
[4] J.S. Yang, S.M. Dong, C.Y. Xu, Mechanical response and microstructure of 2D carbon fiber reinforced ceramic matrix composites with SiC and Ti_3SiC_2 fillers, Ceram. Int. 42 (2016) 3019–3027.
[5] T. Tanaka, N. Tamari, I. Kondo, Fabrication of three-dimensional Tyranno fiber reinforced SiC composite by the polymer precursor method, Ceram. Int. 24 (1998) 365–370.
[6] K. Nakano, A. Kamiya, et al., Fabrication and mechanical properties of carbon fiber reinforced silicon carbide composites, J. Ceram. Soc. Jpn. 100 (1992) 472–475.
[7] V. Michael, C. Anthony, R.C. Robinson, D.J. Thomas, Ceramic Matrix Composite Vane Subelement Testing in a Gas Turbine Environment, ASME GT2004-53970, 2004.
[8] F. Satta, G. Tanda, Effect of discrete-hole arrangement on film-cooling effectiveness for the endwall of a turbine blade cascade, Appl. Therm. Eng. 91 (2015) 507–514.
[9] E. Ghasemi, S. Soleimani, C.X. Lin, Secondary reactions of turbulent reacting flows over a film-cooled surface, Int. Commun. Heat Mass Transfer 55 (2014) 93–101.
[10] J.S. Mayhew, J.W. Baughn, A.R. Byerley, The effect of freestream turbulence on film cooling adiabatic effectiveness, Int. J. Heat Fluid Flow 24 (2003) 669–679.
[11] R.J. Goldstein, E.R.G. Eckert, F. Burggraf, Effect of hole geometry and density on three-dimensional film cooling, Int. J. Heat Mass Transfer 17 (1974) 595–607.
[12] M.G. Ghorab, Film cooling effectiveness and heat transfer analysis of a hybrid scheme with different outlet configurations, Appl. Therm. Eng. 63 (2014) 200–217.
[13] N.M. Yusop, A.H. Ali, M.Z. Abdullah, Computational study of a new scheme for a film-cooling hole on convex surface of turbine blades, Int. Commun. Heat Mass Transfer 43 (2013) 90–99.
[14] A. Azzi, B.A. Jubran, Numerical modelling of film cooling from converging slot hole, Heat Mass Transfer 43 (2007) 381–388.
[15] Y. Yao, J.Z. Zhang, X.M. Tan, Numerical study of film cooling from converging slot-hole on a gas turbine blade suction side, Int. Commun. Heat Mass Transfer 52 (2014) 61–72.
[16] Y. Yao, J.Z. Zhang, Investigation on film cooling characteristics from a row of converging slot-holes on flat plate, Sci. China Technol. Sci. 54 (2011) 1793–1800.
[17] J.D. Heidmann, A.J. Kassab, E.A. Divo, F. Rodriguez, E. Steinthorsson, Conjugate Heat Transfer Effects on a Realistic Film-Cooled Turbine Vane, ASME GT2003-38553, 2003.
[18] M. Silieti, A.J. Kassab, E. Divo, Film cooling effectiveness: comparison of adiabatic and conjugate heat transfer CFD models, Int. J. Therm. Sci. 48 (2009) 2237–2248.
[19] W. Ai, T.H. Fletcher, Computational analysis of conjugate heat transfer and particulate deposition on a high pressure turbine vane, ASME J. Turbomach. 134 (2012) 041020.
[20] R.H. Ni, W. Humber, G. Fan, P.D. Johnson, J. Downs, J.P. Clark, P.J. Koch, Conjugate Heat Transfer Analysis of a Film-cooled Turbine Vane, ASME, GT2011-45920, 2011, 12 pp.
[21] E. Papanicolaou, D. Giebert, R. Koch, A. Schulz, A conservation-based discretization approach for conjugate heat transfer calculations in hot-gas ducting turbomachinery components, Int. J. Heat Mass Transfer 44 (2011) 3413–3429.
[22] M. Zdzislaw, H.R. Alejandro, G.I. Rafael, L.R. Alberto, Analysis of conjugate heat transfer of a gas turbine first stage nozzle, Appl. Therm. Eng. 26 (2006) 1796–1806.
[23] B. Mutnuri, Thermal Conductivity Characterization of Composite Materials, West Virginia University, 2006.
[24] T. Tian, D.C. Kevin, Anisotropic thermal conductivity measurement of carbon-fiber/epoxy composite materials, Int. J. Heat Mass Transfer 55 (2012) 6530–6537.
[25] T. Behzad, M. Sain, Measurement and prediction of thermal conductivity for hemp fiber reinforced composites, Polym. Eng. Sci. 10 (2007) 977–983.
[26] Y.B. Xu, K. Yagi, Automatic FEM model generation for evaluating thermal conductivity of composite with random materials arrangement, Comput. Mater. Sci. 30 (2004) 242–250.
[27] T. Borca-Tasciuc, A.R. Kumar, G. Chen, Data reduction in 3ω method for thin-film thermal conductivity determination, Rev. Sci. Instrum. 72 (2001) 2139–2147.
[28] T.S. Zhu, E. Ertekin, Phonon transport on two-dimensional grapheme/boron nitride superlattices, Phys. Rev. B 90 (2014) 195209.
[29] T.S. Zhu, W.J. Ye, Theoretical and numerical studies of non-continuum gas-phase heat conduction in micro/nano devices, Numer. Heat Transfer, Part B 57 (2010) 203–226.
[30] H.W. Liu, K. Xu, T.S. Zhu, W.J. Ye, Multiple temperature kinetic model and its applications to micro-scale gas flows, Comput. Fluids 67 (2012) 115–122.
[31] K. Xu, A gas-kinetic BGK scheme for the Navier-Stokes equations and its connection with artificial dissipation and Godunov method, J. Comput. Phys. 171 (2001) 289–335.
[32] N.M. Yusop, A.H. Ali, M.Z. Abdullah, Conjugate film cooling of a new multi-layer convex surface of turbine blades, Int. Commun. Heat Mass Transfer 45 (2013) 86–94.
[33] M.Z. Chen, Fundamentals of Viscous Fluid Dynamics, High Education Press, Beijing, 2002.
[34] D.K. Walters, J.H. Leylek, Impact of film-cooling jets on turbine aerodynamic losses, ASME J. Turbomach. 122 (2000) 537–545.
[35] R. Tangemann, W. Gretler, The computation of a two-dimensional turbulent wall jet in an external stream, J. Fluids Eng. 123 (2001) 154–157.
[36] M.J. Fly, B.J. Jubran, A numerical evaluation on the effect of sister holes on film cooling effectiveness and the surrounding flow filed, Heat Mass Transfer 45 (2009) 1435–1446.
[37] ANSYS Inc., ANSYS FLUENT Theory's Guide, Release 14, USA, 2011.
[38] M. Wolfshtein, The velocity and temperature distribution of one-dimensional flow with turbulence augmentation and pressure gradient, Int. J. Heat Mass Transfer 12 (1969) 301–318.
[39] Y. Ree, J.R. Lin, J.G. Zhu, Coordinate transformation uncertainty analysis in larger-scale metrology, IEEE Trans. Instrum. Meas. 64 (2015) 2380–2388.
[40] C. Bianchini, L. Andrei, A. Andreini, B. Facchini, Numerical benchmark of nonconventional RANS turbulence models for film and effusion cooling, ASME J. Turbomach. 135 (2013) 041026.
[41] A.K. Sinha, D.G. Bogard, M.E. Crawford, Film-cooling effectiveness downstream of a single row of holes with variable density ratio, ASME J. Turbomach. 113 (1991) 442–449.